ISSN 0869-5911, Petrology, 2019, Vol. 27, No. 1, pp. 1–16. © Pleiades Publishing, Ltd., 2019.
Russian Text © A.G. Simakin, E.V. Kislov, T.P. Salova, O.Yu. Shaposhnikova, A.N. Nekrasov, 2019, published in Petrologiya, 2019, Vol. 27, No. 1, pp. 4–18.

Reduced CO_2 Fluid as an Agent of Ore-Forming Processes: A Case Study of Dolomite-Replacement Skarns at the Yoko-Dovyren Massif

A. G. Simakin[a, b, *], E. V. Kislov[c], T. P. Salova[a], O. Yu. Shaposhnikova[a], and A. N. Nekrasov[a]

[a] *Korzhinskii Institute of Experimental Mineralogy (IEM), Russian Academy of Sciences, Chernogolovka, Moscow oblast, 142432 Russia*

[b] *Schmidt Institute of Physics of the Earth (IFZ), Russian Academy of Sciences, Moscow, 123242 Russia*

[c] *Geological Institute, Siberian Branch, Russian Academy of Sciences, Ulan-Ude, 670042 Buryat Republic, Russia*

**e-mail: simakin@iem.ac.ru*

Received February 14, 2018; revised April 22, 2018; accepted August 18, 2018

Abstract—The paper presents newly obtained geochemical data on outer-contact rocks and carbonate-replacement skarns of the Yoko-Dovyren layered ultramafic–mafic intrusion in the northern Baikal area. The rocks initially contained CO_2-rich fluid with a high oxygen fugacity (up to NNO + 3–4), which was generated by the partial decomposition of dolomite and by reactions between SiO_2 and carbonates. The skarn blue diopside is enriched in Pt (up to 0.2 ppm) and V (300 ppm), and the wollastonite zone of the skarns contains elevated Re concentrations (up to 0.4 ppm). The REE pattern of the contact-zone quartzite is identical to the REE patterns of phlogopite-bearing lherzolites from the lower contact part of the Yoko-Dovyren massif. These geochemical features of the rocks of the intrusion may be explained by the transfer and redeposition of material by reduced H_2O–CO_2 fluid. According to thermodynamic calculations, a reaction between H_2O–CO_2 fluid and high-Mg olivine at a subsolidus temperature of $T = 950$°C and pressure $P = 2$ kbar should result in a decrease in the oxygen fugacity to QFM – 2 and, hence, generate much CO. According to the calculations, a low oxygen fugacity (close to QFM + 0.7) can also be maintained by pyrrhotite oxidation with H_2O and CO_2 fluid components under cumulus P–T parameters. As a result of these reactions, the fluid should enrich in Pt extracted from magmatic sulfides, and this Pt can be redeposited in rocks, including those composing the skarn zones.

Keywords: Yoko-Dovyren intrusion, platinum, blue diopside, carbon monoxide, skarn, thermodynamic simulations

DOI: 10.1134/S086959111901003X

INTRODUCTION

The Yoko-Dovyren layered mafic–ultramafic intrusion is spatially constrained to the southern margin of the Siberian craton and is an element of the Synnyr volcano-plutonic structure dated at 700–760 Ma (Konnikov et al., 1999). The U–Pb zircon age of the intrusion is 728 ± 3 Ma (Ariskin et al., 2013). PGE mineralization was discovered in the near-bottom Cu–Ni orebodies of the Yoko-Dovyren intrusion in the 1950s. The whole cross-section through the monoclinally tilted intrusion approximately 3.5 km thick, from the bottom ultramafic rocks to near-top granophyres, crops out at the modern erosion surface (Fig. 1). A number of other reefs of low-sulfide mineralization were lately discovered near the boundary between the ultramafic rocks and troctolites. Although the proved ore resources of the Yoko-Dovyren intrusion are relatively small, this intrusion is studied much more comprehensively than many other ultramafic–mafic intrusions in Russia.

The intrusion was thought to be emplaced (before its tilting to a monoclinal setting late during the tectonic deformations) at a depth of 1.7 km, based on the data on the skarn-forming processes and geological reconstructions ($P = 500$ bar) (Pertsev and Shabynin, 1978). Because the cross section of the Yoko-Dovyren intrusion is large (thickness × major axis = 3.5 × 26 km) (Fig. 1) and judging from the mechanical stability, the intrusion should have been emplaced at a depth greater than 1.7 km. Based on gravimetric data, Altukhov et al. (1990) concluded that rocks of elevated density should occur at depths of 25, 18, 11, and 5 km beneath this intrusion. These inferences are consistent with the origin of a number of intermediate magmatic chambers, among which the Yoko-Dovyren occurred at the shallowest depth. Below we present a revised

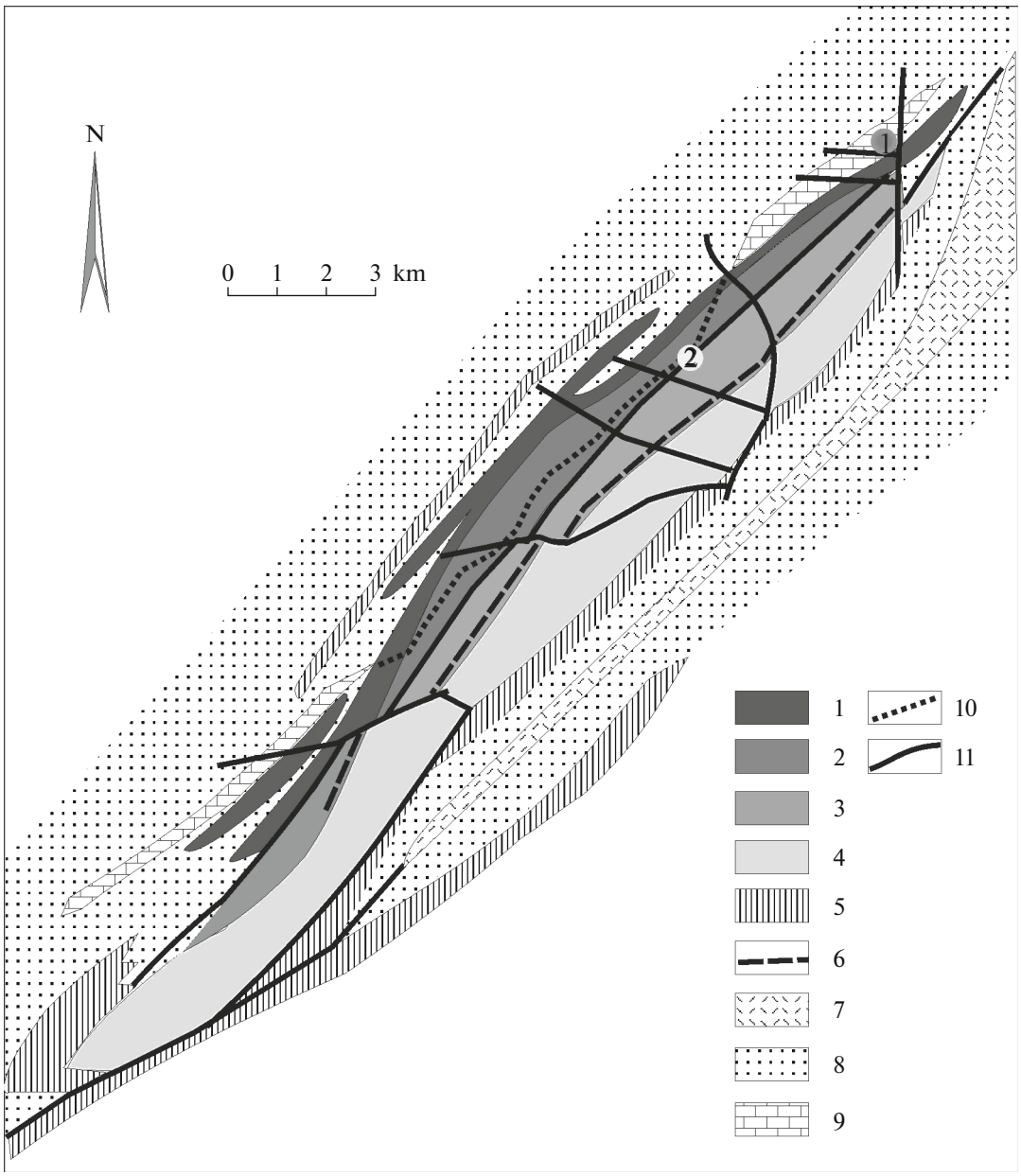

Fig. 1. Schematic geological map of the Yoko-Dovyren layered intrusion and its platiniferous reef (Reef I). (*1*) Plagioclase peridotites; (*2*) plagioclase dunites and wehrlites; (*3*) rhythmically alternating plagioclase dunites, troctolites, and olivine gabbro; (*4*) olivine gabbro and gabbronorites; (*5*) granophyre gabbronorite sills; (*6*) platiniferous horizons (Reef I); (*7*) volcanic rocks (trachyliparites, trachydacites, and andesites); (*8*) quartzites, shales, and sandstones; (*9*) carbonate rocks; (*10*) carbonate-replacement skarns; (*11*) faults. Numerals label sampling sites: (*1*) of host dolomite and quartzite, (*2*) of diopside–calcite–wollastonite skarn.

and refined estimate of the crystallization depth of the intrusion derived from the composition of its magmatic amphibole.

During the crystallization of the Yoko-Dovyren magma, PGE were concentrated in sulfides (Ariskin et al., 2016). Some researchers (Mathez, 1995; Ballhaus and Stumpfl, 1986; Boudreau and Meurer, 1999; Aird and Boudreau, 2013) believe that a significant role in the origin of the platinum-bearing reefs of the Bushveld and Stillwater massifs, which are genetically similar to the platinum-bearing reef of the Yoko-Dovyren intrusion, was played by subsolidus reactions between the cumulus and fluid. It is hypothesized that PGE can be released from sulfide during the early postmagmatic stage as a result of reactions between aqueous fluid and the sulfide-bearing cumulus (Boudreau and Meurer, 1999) and then be redeposited in reefs. A pure H_2O composition of the fluid is in conflict with high

concentrations of hydrocarbons in the platiniferous reef of the Yoko-Dovyren intrusion (Konnikov et al., 2000). A horizon with carbonate-replacement skarns is traced across the whole intrusion (Fig. 1). The composition of the fluid was modified by CO_2 released as a consequence of skarn-forming reactions at magmatic contact with dolomite (Wenzel et al., 2002) and by decarbonation reactions in the thermal aureole of the intrusion. To understand the mechanisms of metasomatic PGE transfer, it is important to estimate the bulk composition of the fluid, oxygen fugacity fO_2 in the fluid, and the proportions of components in this fluid.

We have acquired new data on the composition of minerals and rocks of the diopside skarns and the protolithic dolomite and quartzite in the outer contact zones of the intrusion. These data and results of our thermodynamic simulations allowed us to follow the variations in the P–T parameters and composition of the fluid when the skarns were produced. We have demonstrated that after their reduction, the carbon-bearing fluids actively transported Pt, Ag, V, and Cr and thus produced elevated Pt concentration in the blue diopside. The mechanism suggested below for Pt mobilization from magmatic sulfides is confirmed by thermodynamic calculations of reactions between H_2O–CO_2 fluid and olivine from the magmatic cumulus at a pressure of 2 kbar and a temperature near the solidus (950°C).

ANALYTICAL AND CALCULATION TECHNIQUES

The compositions of rocks and minerals were analyzed by V.K. Karandashev at the Analytical Certification–Test Center of the Institute of Problems of the Technology of Microelectronics and Ultrapure Materials, Russian Academy of Sciences, in Chernogolovka, Moscow oblast. The accuracy of the analyses was checked against a standard reference sample of essexite gabbro SGD-2A (GSO-8670-2005). Minerals were analyzed at the Institute of Experimental Mineralogy, Russian Academy of Sciences, by a TESCAN Vega TS5130MM electron microscope equipped with an INCA Energy 450 analytical EDS system at 20 kV accelerating voltage, 180 pA electron absorption current at a Co standard, and a beam ~0.150 μm in diameter.

Thermodynamic calculations in this paper are of illustrative character, demonstrate the possible evolution of the natural processes, and are not claimed to be highly precise. These calculations were carried out using the thermodynamic database (Holland and Powell, 1998) and, where specified, the database (Robie et al., 1978) with the Maple 9.5 software. Equations of the law of mass action were resolved analytically in simple instances and numerically for multicomponent fluids. The thermodynamic calculations of equilibria in fluids were carried in approximations of ideally mixing nonideal components, with fugacity coefficients for CO, H_2, CH_4, COS, and H_2S were assumed according to (Shi and Saxena, 1992). The fugacity coefficients of H_2O and CO_2 were calculated with regard for the nonideality of mixing according to (Duan and Zhang, 2006; on-line calculations http://models.kl-edi.ac.cn/models/h2o_co2/index.htm), and the low concentrations of other components were neglected.

DATA ON ROCKS AND MINERALS

We have studied diopside skarn samples from E.G. Konnikov's collection, which were taken in carbonate-replacement skarn in the troctolite–plagiodunite zone (Belyi Creek). For comparison, we have also studied the carbonate protoliths sampled by E.V. Kislov in the bottom contact zone of the Yoko-Dovyren intrusion during the 2015–2016 fieldwork (see Fig. 1 for sampling sites).

Host rocks. XRD analysis of samples collected along a traverse near the lower contact of the Yoko-Dovyren intrusion has shown that the dolomite is partly decomposed into periclase (which was later hydrated into secondary platy brucite) and calcite, analogously to what is described in (Wenzel et al., 2002)

$$CaMg(CO_3)_2 = MgO + CaCO_3 + CO_2. \quad (1)$$

At a pressure of 2 kbar and $X_{CO_2} = 1$, decomposition takes place at 850°C. Primary brucite is formed at a low carbon dioxide mole fraction (for example, at 1 kbar and $X_{CO_2} < 0.1$; Ganino et al., 2013). The degree of decomposition decreases at the terminal sampling site at a distance of 10 m away from the contact. Microprobe analyses of the carbonates allowed us to find rare inclusions of lizardite $Mg_3Si_2O_9(OH)_2$, ilmenite, magnetite, and pyrrhotite. The calcite contains 2–3 mol % $MgCO_3$, which corresponds to equilibrium of these minerals at low temperatures. We have also examined a quartzite bed in the carbonate unit. The quartzite was sampled at a distance of 100 m away from the contact. The silica concentration in the quartzite is close to 92%. The rocks also contain silicate minerals, which were identified using a microprobe: chlorite, prehnite, muscovite, as well as accessory zircon, rutile, and pyrrhotite (Fig. 1). Of great interest are finds of zinc phases: zinc ilmenite and zinc silicate. The presence of prehnite in the mineral assemblage corresponds to the low-temperature (retrograde) greenschist facies: $T = 200$–300°C, $P = 2$–3 kbar (Frey and Robinson, 1999). The occurrence of the Zn phases indicates that the concentration of this element in the circulating fluid was fairly high.

Blue diopside. The carbonate-replacement skarns occur within the intrusion, and their maximum crystallization temperatures were close to the magmatic

ones. The skarns have been studied since the 1960s (Kislov et al., 1998), and the process that produced the magnesian skarns was studied most thoroughly. These skarns consist of brucite (pseudomorphs after periclase), olivine, and spinel (Wenzel et al., 2002) and were produced at maximal heating to 1100°C, which triggered calcite melting. We have studied samples of the diopside–calcite–wollastonite skarn from blocks of brucite skarn in the troctolite. According to ICP-MS analyses (Table 2), the blue diopside zone has the maximum Mg/Ca = 0.81, and a cutting bleached zone rich in calcic silicates has Mg/Ca = 0.72. Both zones are enriched in Ca relative to the protolithic dolomite, whose Mg/Ca = 1.02 ± 0.02. The bleached zone shows evidence of silica removing, as follows from the assemblage of monticellite $Mg_{0.94}Ca_{1.06}SiO_4$ and redeposited diopside. The blue diopside crystals are equant and as large as 1 mm (Fig. 2a). The diopside sometimes hosts inclusions of anhydrous Ca silicate of the composition $Ca_5Si_4O_{13}$ and wollastonite crystals. The crystals of the redeposited diopside are elongate, 2–5 μm in cross section, and up to 150 μm long (Fig. 2b). High fluorine and low water activities in the fluid involved in the origin of the bleached zone follow from the presence of water free cuspidine $Ca_4(Si_2O_7)F_2$. According to microprobe analyses, the monticellite contains fluorine (likely in the form of microfluid inclusions): up to 0.2–0.6 wt %. Later Ca introduction is reflected in the overprinted crystallization of rankinite $Ca_3Si_2O_7$, which is found as large crystals in the bleached zone and fine-grained masses filling fractures between blue diopside crystals. A likely reason for the low analytical totals of microprobe analyses of the rankinite is its partial secondary hydration with the origin of afwillite $Ca_3(SiO_3OH)_2 \cdot 2H_2O$. Apatite crystals in the rankinite have elevated fluorine and relatively low hydroxyl concentrations: $Ca_5(PO_4)_3(OH_{0.05\text{-}0.11},F_{0.87\text{-}0.93},Cl_{0.02})$. Apatite from the monticellite–diopside zone contains the carbonate ion and more hydroxyl, chlorine, and sulfur: $Ca_5(PO_4)_{2.69}(CO_3)_{0.29}(SO_4)_{0.02}(OH_{1.15},F_{0.12},Cl_{0.04})$. The composition of the apatite reflects an increase in the fluorine concentration in the late fluid, as was previously mentioned in (Kislov, 1998).

The reason for the blue color of the diopside is its high concentration of (VO^{2+}), which substitutes Ca. Vanadium occurs in nature mostly in valence forms of V^{3+}, VO^{2+}, which have characteristic color both in aqueous solutions and in minerals: green for V^{3+} and blue for VO^{2+} (see for example, Satake and Mido, 2010). Cavansite and pentagonite $Ca(VO)Si_4O_{10} \cdot 4(H_2O)$, vanadium minerals found in nature, have a color close to that of the blue diopside. The V^{3+}/V^{4+} ratio depends on the oxygen fugacity, and this makes it possible to use the V distribution coefficient between crystalline phases (for example, olivine and spinel) and melt as a tool for measuring oxygen fugacity. The distribution coefficient between the olivine and melt $K_{D,V}$ is close to 0.25 (depending on the oxygen fugacity), which corresponds to the stoichiometry of the reaction $V^{3+} + 1/4O_2 = V^{4+} + 1/2O^{2-}$ (Canil and Fedortchouk, 2001). To change the V^{3+}/V^{4+} ratio by one order of magnitude, the oxygen fugacity has to be changed by four orders of magnitude (for example, from NNO + 3 to QFM).

The average vanadium concentration in the diopside crystals (16 spot spectrometric analyses) is 345 ppm. Microprobe profile across the crystals reveal a zonal vanadium distribution in the diopside with a decrease in the vanadium concentration to value below the detection limit in the grain margins with the paler zones and intergranular boundaries. Some of the zones visible in BSE images are correlated with the V concentrations, while others do not (Fig. 2a). It should be mentioned that some spot analyses of the diopside show comparably high Ti concentrations. The Fe, Cr, and Mn concentrations are much lower. Both ICP-MS analyses of the diopside bed yielded similar vanadium concentrations of 300–350 ppm. Vanadium concentrations in the recrystallized diopside and its aggregates with monticellite are at the detection limit of the microprobe.

Trace-element composition of the skarns and contact zones. ICP-MS analytical techniques widens the circle of analyzable elements (Table 2). In addition to the aforementioned enrichment of the diopside skarns in vanadium, it should be mentioned (Table 1) that the rocks are enriched in platinum (0.18 and 0.034 ppm) and silver (0.28 and 0.057 ppm). It is interesting to note that the vanadium concentrations are close to an average level of 300 ppm, whereas the platinum and silver concentrations show significant coupled variations. Arsenic behaves in a similar manner (2.1 and 0.93 ppm). The cadmium concentrations are at a maximum in the diopside zone but do not correlate with the platinum concentration (0.19 and 0.26 ppm). The bleached zone is typically poor in vanadium (7–6 ppm) and relatively rich in chromium (98–88 ppm). It is enriched in rhenium (0.38, 0.40 ppm), whose concentrations in the rest of the analyzed rocks are below the detection limits, but the zone is depleted in silver (<0.02 ppm) and platinum (<0.006 ppm). It should also be mentioned that this zone is relatively enriched in molybdenum (1 as compared to 0.6 ppm in the blue diopside) and tungsten (11.5 against 0.7–0.8 ppm). Another trait of the bleached zone is the low Nb concentration and Nb/Ta = 3, as compared to "normal" Nb/Ta = 13–15 of all other rocks and minerals (carbonates, quartzite, and blue diopside). This feature may be explained by the effect of fluorine, which forms more stable compounds with Nb and facilitates its removal. The quartzite and the carbonate samples collected at the greatest distances from the contact bear relatively low concentrations of zinc (26.7, 34.2 ppm) and silver but higher concentrations of lead (7.7, 15.8 ppm), and

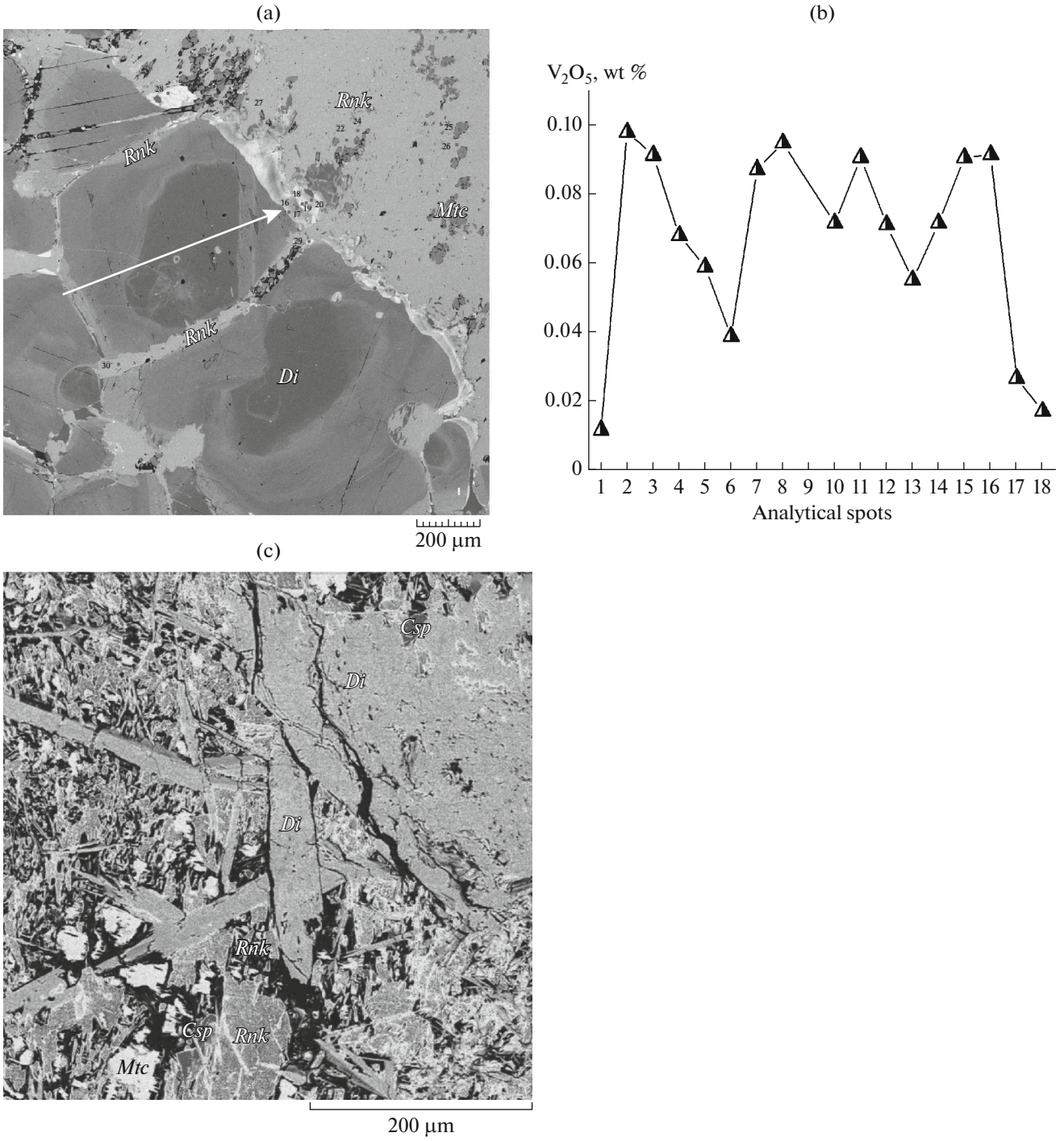

Fig. 2. BSE images of diopside from the skarn. (a) Zoned crystals of blue diopside, the arrow points to the profile along which V concentration was analyzed. Secondary rankinite fills cracks between diopside crystals and replaces the fine-grained zone with monticellite. (b) Profile showing the variations in V concentration across a crystal of the blue diopside (see the arrow in Fig. 2a). Vanadium concentrations decrease toward the margins. (c) Diopside–monticellite recrystallization zone with retrograde rankinite. Minerals: *Mtc*—monticellite, *Rnk*—rankinite, *Di*—diopside, *Csp*—cuspidine $Ca_4(Si_2O_7)(OH,F)_2$.

the quartzite is maximally enriched in lithium (19.8 ppm) and chromium (261 ppm).

The compositions of the skarns and host rocks are shown in a general form in Fig. 3. Note that the REE patterns of all of the rocks are similar: they are flat at HREE, with a mild increase in the normalized Er concentration in the carbonates, and with a linear increase at LREE (Fig. 3a). The total REE concentrations are

Table 1. Composition of minerals from the Yoko-Dovyren massif

Carbonates in the outer-contact zone

Component	Brucite (5)		Dolomite (8)		Calcite(5)		Serpentine (7)		Ilmenite (3)		Magnetite (5)	
	C, wt %	1σ	*C*, wt %	1σ	*C*, wt %	1σ	*C*, wt %	1σ	*C*, wt %	1σ	*C*, wt %	1σ
SiO_2	–	–	–	–	0.08	0.06	41.31	1.43	–	–	–	–
TiO_2	–	–	–	–	–	–	0.20	0.16	63.33	0.78	0.11	0.11
Al_2O_3	0.13	0.11	–	–	–	–	2.84	1.09	0.10	0.09	0.08	0.05
Cr_2O_3	–	–	–	–	–	–	0.12	0.14	0.15	0.15	0.09	0.08
FeO	0.45	0.06	0.03	0.06	0.27	0.13	0.67	0.12	16.14	0.53	86.06	3.41
MnO	–	–	0.06	0.09	–	–	–	–	3.72	0.21	–	–
MgO	59.78	0.62	19.57	1.51	1.02	0.68	40.88	1.01	20.35	0.69	1.78	0.23
CaO	0.09	0.06	32.13	1.05	54.49	0.70	0.19	0.14	0.39	0.05	–	–
Na_2O	–	–	–	–	–	–	–	–	–	–	–	–
K_2O	–	–	–	–	–	–	–	–	–	–	–	–

Quartzites in the outer-contact zone

Component	Muscovite (3)*		Prehnite (5)		Chlorite (5)		Zircon (4)		Zn–Ilmenite (3)		Zn–silicate (1)	
SiO_2	44.91	0.34	38.16	2.95	27.57	1.39	30.93	0.62	0.47	0.12	28.23	–
TiO_2	0.10	0.09	–	–	0.11	0.09	–	–	51.76	54.21	–	–
Al_2O_3	30.89	0.12	27.31	1.15	20.91	1.09	0.04	0.04	0.33	0.24	5.68	–
Cr_2O_3	–	–	0.04	0.06	0.27	0.31	0.05	0.08	0.49	0.00	0.84	–
FeO	1.05	0.17	–	–	20.96	1.22	0.21	0.11	24.82	16.52	0.8	–
MnO	–	–	0.15	0.10	0.30	0.19	0.17	0.06	8.65	6.44	0.05	–
NiO	–	–	–	–	–	–	0.12	0.10	–	–	–	–
ZnO	–	–	–	–	–	–	–	–	10.84	20.81	49.3	–
MgO	1.29	0.07	0.06	0.06	10.66	0.64	–	–	0.00	0.23	2.31	–
CaO	0.06	0.04	23.83	0.95	0.13	0.11	–	–	0.00	0.00	–	–
Na_2O	0.22	0.15	–	–	–	–	–	–	1.66	2.93	6.15	–
K_2O	11.25	0.05	–	–	–	–	–	–	–	–	–	–
ZrO_2	–	–	–	–	–	–	64.12	0.99	–	–	–	–
HfO_2	–	–	–	–	–	–	1.59	0.26	0.75	0.74	–	–

Composition of skarn minerals

Component	Diopside (10)		Monticellite (9)		Rankinite (5)		Wollastonite (1)		$Ca_5Si_4O_{13}$ (1)		Apatite (1)		Cuspidine (1)	
SiO_2	53.04	0.85	36.76	0.53	40.28	0.60	49.55	–	46.08	–	1.75	–	31.95	–
TiO_2	0.06	0.05	0.03	0.05	–	–	–	–	–	–	0.23	–	–	–
Al_2O_3	0.15	0.09	0.14	0.06	0.07	0.07	–	–	0.14	–	–	–	0.14	–
Cr_2O_3	–	–	–	–	0.17	0.23	–	–	–		–	–	–	–
FeO	0.05	0.08	0.10	0.07	–	–	–	–	–	–	0.14	–	–	–
MnO	0.06	0.07	–	–	–	–	–	–	–	–	–		–	
MgO	17.38	0.45	23.91	0.39	0.25	0.39	0.21	–	0.09	–	0.2		0.18	
CaO	27.08	0.18	37.86	0.39	53.95	0.85	50.60	–	53.19	–	56.39	–	63.7	–
Na_2O	0.10	0.06	0.09	0.07	–	–	–	–	0.16	–	0.02	–	–	–
K_2O	0	–	–	–	–	–	–	–	–	–	0.06	–	–	–
F	0	–	0.27	0.19	0.38	0.32	–	–	0	–	0.45	–	10.0	–
Cl	0	–	–	–	–	–	–	–	–	–	0.26	–	–	–
P_2O_5	0	–	–	–	–	–	–	–	–	–	38.65	–	–	–
S	0	–	–	–	–	–	–	–	–	–	0.32	–	–	–

* Numerals in parentheses specify the number of the averaged analyses.

Table 2. Composition of the skarns and contact rocks

Component	Carbonate 1	Carbonate 2	Quartzite	Blue diopside	Blue diopside	Bleached zone in blue diopside	Bleached zone in blue diopside
SiO_2	–	–	91.5	55.20	54.84	–	–
TiO_2	0.039	0.026	0.35	0.1	0.027	0.0075	0.0072
Al_2O_3	0.48	0.36	3.6	0.050	0.079	0.11	0.059
Fe_2O_3	0.26	0.11	1.7	0.075	0.11	0.13	0.12
MnO	0.026	0.014	0.042	0.0039	0.0051	0.011	0.011
MgO	26.6	25.2	0.71	16.3	16.4	18.1	17.9
CaO	35.6	35.3	1.6	28.1	28.4	34.7	34.1
Na_2O	0.014	0.016	0.039	0.053	0.039	0.014	0.012
K_2O	0.0080	0.0059	0.12	0.014	0.015	0.011	0.0067
P_2O_5*	0.15	0.27	0.015	0.041	0.018	0.051	0.047
S_{tot}	0.004	b.d.l.	0.0034	0.021	0.0064	b.d.l.	b.d.l.
H_2O**	7.57	6.27		–	–		
Li	1.6	1.0	19.8	0.33	0.39	3.7	3.0
Be	1.0	0.25	0.71	0.13	0.19	2.0	1.6
Sc	0.65	0.44	3.2	0.27	0.32	0.15	0.14
V	5.3	9.2	19.4	300	345	7.3	6.1
Cr	13.8	32.8	261	3.8	80.2	98.6	88.7
Co	1.0	0.92	2.9	0.79	1.0	1.2	1.2
Ni	9.1	23.4	107	6.3	55.4	68.8	59.9
Cu	8.6	1.3	11.7	3.9	5.9	7.6	7.2
Zn	26.7	7.2	34.2	11.0	6.6	5.8	4.7
Ga	0.43	0.38	5.6	0.15	0.10	0.22	0.21
As	b.d.l.	b.d.l.	0.29	2.1	0.93	4.2	2.1
Rb	0.17	0.15	6.9	0.18	0.38	0.57	0.20
Sr	139	114	41.4	108	118	64.2	65.5
Y	2.8	4.2	10.8	0.25	0.44	0.89	0.43
Zr	27.3	12.6	129	4.0	20.9	2.6	2.3
Nb	1.2	0.75	6	0.12	0.40	0.36	0.32
Mo	0.13	0.32	1.6	0.19	0.68	1.0	1.0
Ag	0.065	b.d.l.	0.052	0.28	0.057	b.d.l.	b.d.l.
Cd	b.d.l.	b.d.l.	b.d.l.	0.19	0.26	0.063	0.062
Sn	0.15	0.082	0.57	0.75	0.51	0.72	0.72
Sb	0.17	b.d.l.	0.15	0.26	0.27	0.89	0.22
Cs	0.23	0.077	0.36	0.040	0.042	0.017	0.014
Ba	7.9	8.5	24.9	3.0	5.8	5.5	2.3
La	1.9	1.5	12.2	0.16	0.13	0.72	0.38
Ce	4.0	4.0	29.7	0.31	0.32	1.5	0.64

Table 2. (Contd.)

Component	Carbonate 1	Carbonate 2	Quartzite	Blue diopside	Blue diopside	Bleached zone in blue diopside	Bleached zone in blue diopside
Pr	0.46	0.41	3.0	0.042	0.035	0.15	0.060
Nd	1.9	1.8	11.4	b.d.l.	0.088	0.77	0.32
Sm	0.42	0.45	2.1	0.035	0.025	0.14	0.050
Eu	0.076	0.083	0.54	0.018	0.010	0.045	0.026
Gd	0.36	0.44	2.0	0.011	0.038	0.17	0.059
Tb	0.059	0.075	0.32	b.d.l.	b.d.l.	0.022	0.0080
Dy	0.41	0.53	2.2	0.025	0.023	0.14	0.051
Ho	0.085	0.12	0.41	0.0068	0.0076	0.025	0.010
Er	0.34	0.43	1.3	0.022	0.028	0.080	0.033
Tm	0.040	0.050	0.21	0.02	0.0038	0.0093	b.d.l.
Yb	0.28	0.33	1.5	0.021	0.029	0.067	0.030
Lu	0.039	0.042	0.23	b.d.l.	0.075	0.041	0.043
Hf	0.61	0.27	3.6	0.08	0.24	0.050	0.034
Ta	0.075	0.060	0.39	b.d.l.	0.13	0.077	0.15
W	0.18	0.34	1.9	0.84	0.69	1.5	1.6
Re	b.d.l.	b.d.l.	b.d.l.	b.d.l.	b.d.l.	0.38	0.40
Pt	b.d.l.	b.d.l.	b.d.l.	0.18	0.034	b.d.l.	b.d.l.
Pb	7.7	3.0	15.8	1.1	1.4	1.9	1.9
Bi	b.d.l.	b.d.l.	0.032	b.d.l.	0.0085	b.d.l.	b.d.l.
Th	0.29	0.61	4.9	0.024	b.d.l.	0.11	0.030
U	0.68	1.7	1.5	0.16	2.36	1.2	1.2

Cells with pale shading correspond to elevated concentrations, and dark gray ones correspond to concentrations below the detection limits (b.d.l.). Concentration of oxides are in wt %, elements are in ppm. * Water concentrations were determined by KFT method.

the lowest in the diopside and the highest in the quartzite. For comparison, Fig. 3a shows the REE patterns of magmatic rocks of the Yoko-Dovyren massif (Ariskin et al., 2015). The REE patterns of the quartzite and ultramafic rocks of the Yoko-Dovyren massif are practically identical. The figure also displays data on the composition of experimental melts generated in the presence of reduced carbon dioxide fluid at $P = 2$ kbar and $T = 1000°C$ (Simakin et al., 2018). Their REE patterns are also practically exactly identical to those of gabbro from the Yoko-Dovyren intrusion. For a broader review, the compositions are normalized to the average crust composition (according to https://earthref.org/GERM), but not to the primitive mantle or chondrite (Fig. 3b). This normalization made the HFSE and REE patterns almost linear for magmatic rocks of the Yoko-Dovyren pluton (with the quartzite practically exactly identical to ultramafic rocks of the Yoko-Dovyren massif) and other studied rocks. At the same time, the variations of the concentrations of LILE, Pb, Th, and U are high. It has been demonstrated that magmatic rocks of the Yoko-Dovyren intrusion are enriched in isotopes from the Archean crust (Ariskin et al., 2015). The data presented above can be interpreted as evidence that the trace-element compositions of the sedimentary and magmatic rocks equalized under the effect of mantle fluid, which was rich in "cratonic components" because of the breakup of the slab at collision. An important role of deep fluid in the territory in question also follows from the isotopic composition of skarns in the outer-contact zone of syenite in the Tazheran massif near Ol'khon Island in the Baikal area. It was determined that the thermal decomposition of the carbonate proceeded with the involvement of a external (not related to carbonate decomposition but from external crustal or mantle sources) reduced carbon (Doroshkevich et al., 2017).

Emplacement depth of the Yoko-Dovyren pluton according to mineralogical barometry. To analyze the

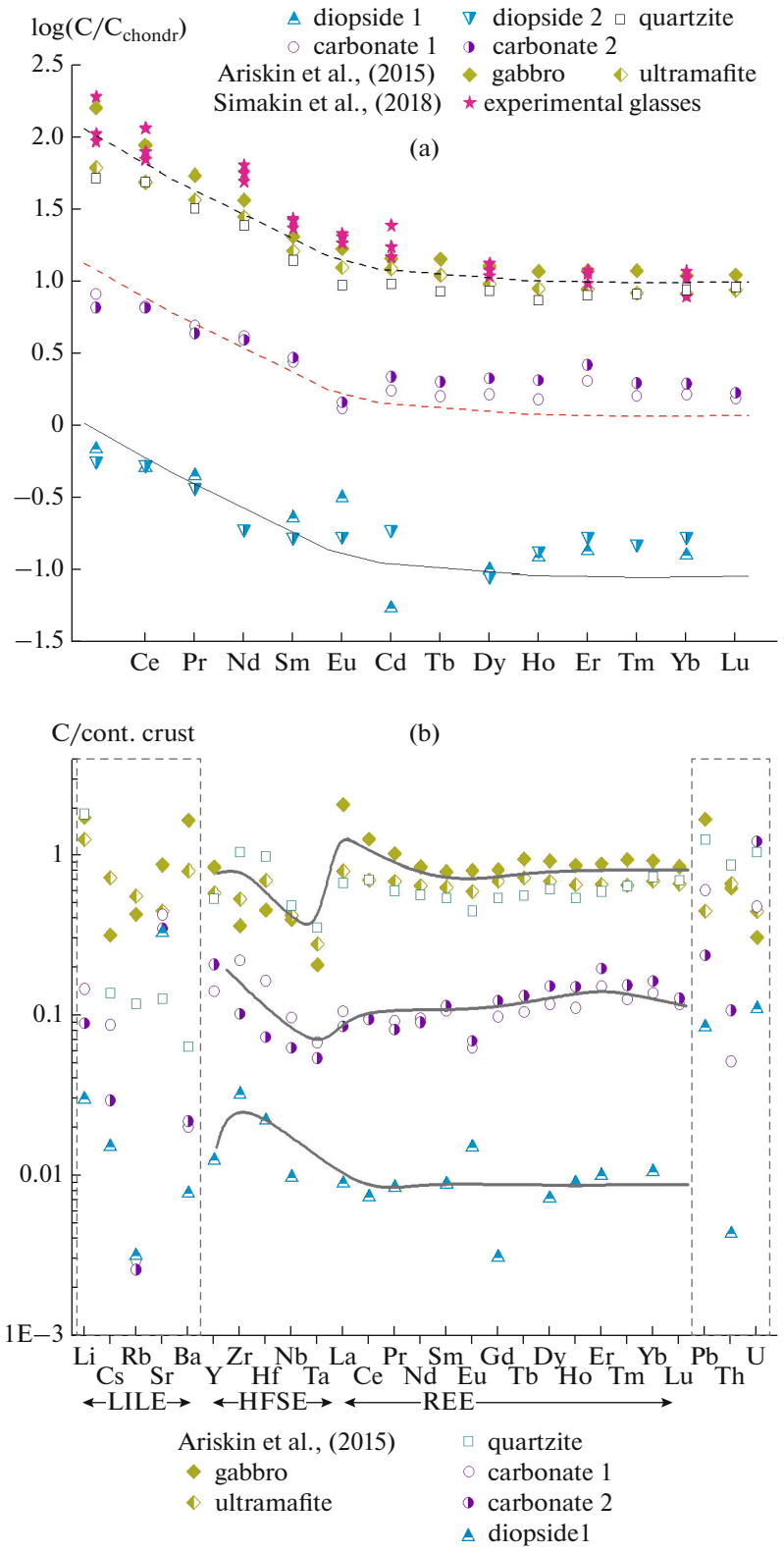

Fig. 3. Geochemical characteristics of the samples and magmatic rocks of the Yoko-Dovyren massif. (a) Chondrite-normalized (Sun and McDonough, 1989) REE patterns of magmatic rocks of the Yoko-Dovyren massif (Ariskin et al., 2015), experimental glasses (Simakin et al., 2018), and samples described in this publication. (b) Continental crust-normalized (https://earthref.org/GERM/) trace-element patterns of the rocks.

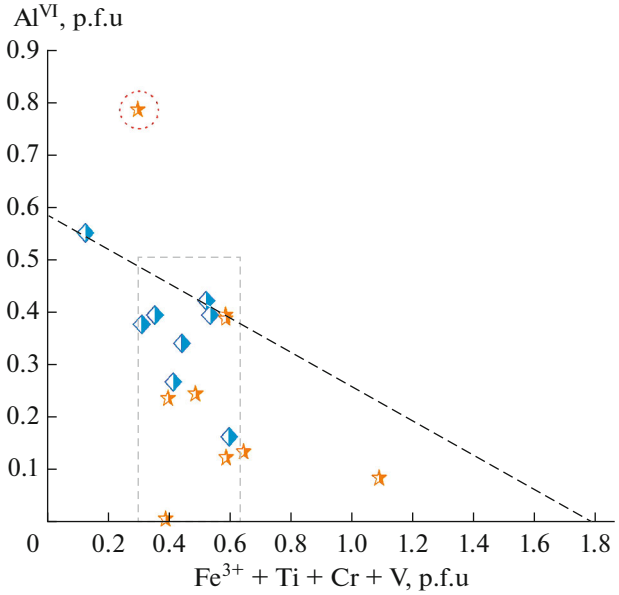

Fig. 4. Al^{VI} vs. Fe^{3+} + Ti + Cr + V diagram (Simakin and Shaposhnikova, 2018) for the composition of amphibole from the Yoko-Dovyren massif: stars are amphibole from the dunites and plagioperidotites (Kislov et al., 1995), diamonds are the mineral from the plagiolherzolites. The circled star corresponds to the composition of the amphibole (autometasomatic or metamorphic) that crystallized from solution.

parameters under which the skarns were produced, the pressure under which the intrusion was emplaced should be evaluated independently of the estimated parameters under which the skarns were formed. Literature data on the compositions of equilibrium clinopyroxene and orthopyroxene in the plagioperidotite zone of the intrusion (Kislov, 1998) make it possible to evaluate the pressure by the two-pyroxene barometer (Putirka, 2005). Only one pair of the compositions in Table 25 in (Kislov, 1998) meets the requirements of equilibrium and yields a pressure of 2.8 kbar. We have analyzed amphibole from the plagioclase lherzolites of the peridotite zone in the bottom part of the Yoko-Dovyren massif. This amphibole is partly replaced by secondary chlorite. The selected amphibole analyses (Table 2) correspond to calcic amphibole, sometimes with elevated concentrations of alkalis ($Na_2O + K_2O$ up to 3.65 wt %). The amphibole is distinguished for unusually high concentration concentrations of V (up to 0.25 wt % V_2O_5) and Cr (up to 2 wt % Cr_2O_3). The pressure was evaluated by the empirical barometer (Simakin and Shaposhnikova, 2017), which was calibrated for high-Mg andesite and mafic melts. A set of eight analyses in a Al^{VI} vs. Ti + Fe^{3+} + V + Cr diagram is constrained by a straight line from above (Fig. 4) that passes exactly through the check point ($Al^{VI} = 0$, Ti + Fe^{3+} + V + Cr = 1.8) and intercepts the ordinate at $Al^{VI}_{max} = 0.6$, which corresponds to a pressure of approximately 2 kbar. The average concentration of polyvalent cations is 0.4, which reflects the relatively low oxygen fugacity during the crystallization of the amphibole (likely close to QFM). The emplacement depth of the intrusion was thus at least 7 km, but not 1.5 km, as was estimated earlier (Pertsev and Shabynin, 1978). This should be taken into account in thermodynamic estimates of the crystallization parameters of rocks of the Yoko-Dovyren intrusion.

THERMODYNAMIC MODEL

Data presented above can be readily interpreted based on results of thermodynamic simulation of the fluid composition during the crystallization of the blue diopside. We have calculated the thermodynamics of the skarn-forming processes to the calcite melting temperature in the approximation of inert CaO and MgO. At a significant silica transfer, as in our situation, this approach is more adequate to describe equilibrium at perfectly mobile silica and carbon dioxide behavior (Ferry et al., 2011). Dolomite can be immediately transformed into diopside, without forming the forsterite–calcite assemblage, at a relatively low temperature, a relatively high CO_2 mole fraction in the fluid, and a high SiO_2 activity (Fig. 5a). The diagram in Fig. 5a is similar to Fig. 8a in (Ferry et al., 2011). At a high temperature (900°C), monticellite can be formed from diopside at silica removal due to a decrease in its activity in the fluid at a relatively high CO_2 activity (0.5–0.3) (Fig. 5b). At a relatively low temperature, the *Di–Mtc* equilibrium is possible only at a very low CO_2 activity (<0.01). Observations indicate that the temperature was no higher than 1000–1100ºC, because otherwise purely magnesian skarns would had been formed because of calcite melting. CO_2, which was generated by the reaction of calcite decomposition, is a strong oxidizer, and hence, V formed the VO^{2+} ion. The latter substituted Ca in the diopside and imparted a blue color to this mineral. The $H_2O–CO_2$ fluid was reduced with time and with an increase in its temperature because of its interaction with the cumulates and ultramafic magma. The outcrop of carbonate-replacement rocks with blue diopside is a few meters across, and hence, the heating of these rocks during the first (and, perhaps, also later) magmatic emplacements was gradual. We do not possess data to reproduce a detailed thermal history and to chart the flow of the fluid. The originally high silica activity was caused by the dissolution of dolomite-hosted chert segregations (Kislov, 1998). When the temperature was high, the silica activity was buffered by the solubility of mafic minerals (first and foremost, olivine) in the cumulus of the ultramafic magma, the dominant intergranular melt. In skarns developing at contacts with silicic magmas (adamellites), silica activity in the fluid is higher, and no assemblages with monticellite are formed (Ferry et al., 2011).

Reduction mechanism of the H_2O–CO_2 fluid. It is widely known that serpentinization of ultramafic rocks is associated with the reduction of the fluids and a significant increase in the hydrocarbon and hydrogen concentrations (Jones et al., 2010). Below we present results of our thermodynamic analysis that indicate that a high-temperature subsolidus reaction of olivine cumulate with H_2O–CO_2 fluid also maintains a low oxygen fugacity. An important crystalline phase involved in subsolidus redox equilibria is spinel containing the magnetite end member.

The reaction of olivine oxidation in the presence of H_2O–CO_2 fluid is written in the general form as

$$Fe_2SiO_{4ss} + 1/3\,O_2 = 2/3\,Fe_3O_{4ss} + SiO_{2fl}, \quad (2)$$

where the fayalite end member occurs as solid solution with forsterite, and silica is dissolved in the fluid. The silica solubility depends on the fluid composition and P–T parameters and, taken together with the fayalite activity in the olivine, unequivocally defines (buffers) the equilibrium oxygen fugacity. The bulk composition of the fluid (for example, in the C–S–H–O system) and oxygen fugacity define the relations between fluid species.

The concentration of ferric iron (according to Kislov, 1998) in some spinels from the ultramafic part of the Yoko-Dovyren massif is very low, and the corresponding mole fraction of the magnetite end member (X_{Mag}) is 0.02 ± 0.008. The rest of the spinels are more oxidized, and their X_{Mag} = 0.15 ± 0.06. The most strongly oxidized spinel posseses X_{Mag} = 0.32 ± 0.06. The iron mole fraction of olivine in the lower ultramafic plagioperidotite and plagiodunite parts of the intrusion is (according to Kislov, 1998) f = 13.89 ± 1.66 and f = 12.57 ± 1.80 in the lower part of the dunite unit. These data on the compositions of the phases can be used to evaluate the oxygen fugacity in equilibrium (2) at T = 950°C and P = 2000 bar.

To calculate the activity of the magnetite end member, we used the thermodynamic model of the spinel solid solution (Sack and Ghiorso, 1991). The activities were calculated for average spinel compositions in its compositional groups, using the on-line calculator involving the latest version of the model (http://melts.ofm-research.org/CalcForms/index.html). The activity coefficient at high magnetite concentrations is 0.5–0.6 and decreases to 0.08 for the most reduced spinels. The calculations were thus carried out with three magnetite activity values (a_{Mag}): 0.002, 0.07, and 0.19. The activity of the fayalite end member in magnesian olivine was calculated with the solid-solution model in (Berman and Aranovich, 1996). The activities of olivine corresponding to the foregoing average compositions are a_{Fa} = 0.038 and 0.044. According to these estimates, the oxygen fugacity at $\log(a_{Qz})$ = –1.3 in equilibrium spinel of the most widely spread composition (X_{Mag}=0.15) was QFM – 2.2 [QFM: $f\mathrm{O}_2 = (-25096.3/T) + 8.735 + 0.11(P - 1)/T$],

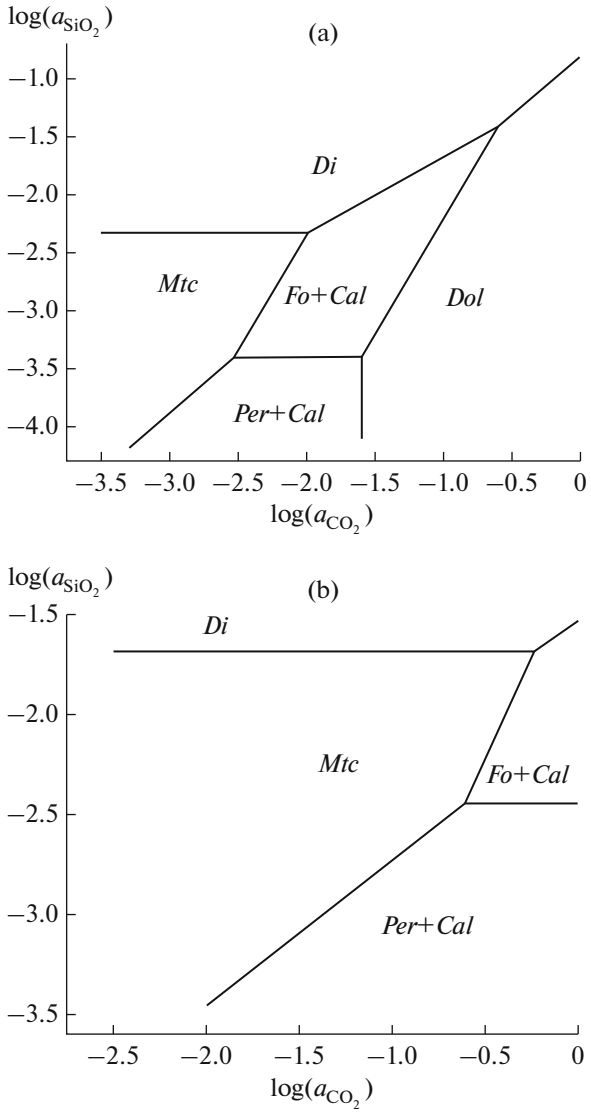

Fig. 5. Phase diagrams for the diopside–monticellite skarns at perfectly mobile silica, P = 2 kbar and (a) 600°C, and (b) T = 950°C. Minerals: *Mtc*—monticellite, *Per*—periclase, *Cal*—calcite, *Dol*—dolomite, *Fo*—forsterite, and *Di*—diopside.

where T is the temperature in K and P is the pressure in bar (Frost, 1991). This estimate is somewhat lower than the oxygen fugacity corresponding to the CCO buffer [QFM – 2.0 at P = 200 MPa and T = 950°C (French and Eugster, 1965)]. If the fluid contains CO_2, this value sets the lower limit for the oxygen fugacity. The most oxidized spinel corresponds to $f\mathrm{O}_2$ close to QFM – 1.3. The most reduced spinel was likely primary magmatic and did not react with the fluid; the equilibrium $f\mathrm{O}_2$ formally calculated from reaction (2) is unbelievably low: QFM – 5.3, i.e., lower than the IW buffer.

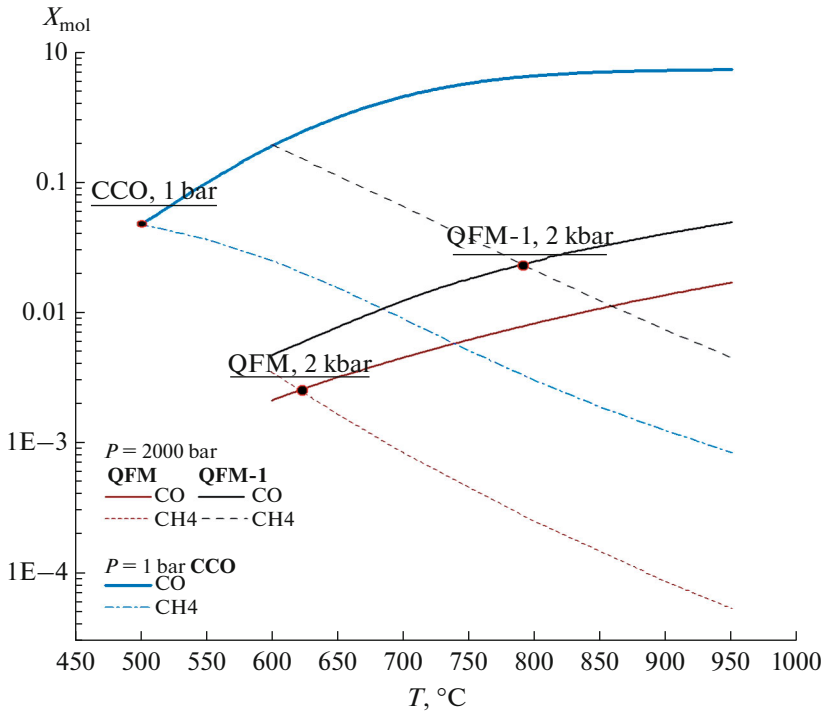

Fig. 6. Calculated CH_4 and CO mole fractions in CO_2–H_2O at the starting fluid composition $X_{H_2O} = X_{CO_2} = 0.5$, $P = 200$ MPa; oxygen fugacity is specified in the diagram. For comparison, the diagram shows concentrations of reduced carbon species in H_2O–CO_2 fluid in equilibrium with graphite at a pressure of 1 bar. Spots in the diagram mark equal CO and CH_4 concentrations.

The predicted oxygen fugacity is qualitatively consistent with the composition of the amphibole (see above). A low oxygen fugacity in the vicinity of the outer contact of the intrusion was evaluated using the ilmenite–magnetite pair from the carbonates (see Table 1 for the compositions). According to calculations with the ILMAT software (Lepage, 2003), the minerals were in equilibrium with each another at $T =$ 398°C and fO_2 close to QFM – 1.9.

The low oxygen fugacity in the olivine cumulus generated reduced gases in the fluid. Neglecting hydrocarbons of high molecular weight in the C–O–H system, we limited our evaluations to H_2O, CO_2, H_2, CH_4, and CO. The oxygen fugacity was assumed to be controlled by buffer reaction (2). Carbon monoxide was an active fluid component, which formed stable π-complexes with transition metals, including PGE. In this sense, methane was a passive component. A temperature increase was associated with the thermal decomposition of CH_4, whereas the CO concentration increased. Figure 6 shows results of the thermodynamic calculations of the dependences of the CO and CH_4 concentrations (mole fractions) on temperature at $P = 2$ kbar and oxygen fugacity $fO_2 =$ QFM and QFM – 1. Also for comparison, this figure displays data on fluid at a pressure of 1 atm in equilibrium with graphite (CCO buffer), with CO concentration of the fluid reaching a maximum and that of CH_4 at a minimum. The ratio $CO/CH_4 = 1$ is reached at a higher temperature and under more reducing conditions ($T \approx$ 750°C at $fO_2 =$ QFM – 1). Thus, at $P = 2$ kbar (as in the magmatic chamber of the Yoko-Dovyren intrusion), high CO concentrations can be anticipated to occur at high temperatures, close to the solidus ones.

Sulfide equilibrium. It is interesting to analyze how H_2O–CO_2 fluid should have reacted with pyrrhotite, the dominant sulfide mineral, which practically completely controls the PGE mineralization after the sulfide melt segregated from the silicate one. Both H_2O and CO_2 are strong oxidizers, which are able to oxidize sulfides. When sulfides react with fluid, PGE are extracted into the solution and can migrate into the cumulus and be accumulated in it. The reaction of pyrrhotite with H_2O–CO_2 fluid was thermodynamically simulated at $P = 2000$ bar and $T = 950$°C. We assumed that the fluid contained the following components of the C–O–S–H system in equilibrium with FeS: (1) H_2O, (2) H_2, (3) CO_2, (4) CO, (5) H_2S, (6) SO_2, (7) COS, (8) O_2, and (9) S_2. For simplicity, we neglected the possible synthesis of CH_4 and thiols. To find the concentrations of the nine components, we used mass-action equations for the following six reactions:

1) $3FeS + 2O_2 = Fe_3O_4 + 3/2\,S_2$,

2) $H_2 + 1/2\,O_2 = H_2O$,

3) $CO + 1/2\,O_2 = CO_2$,

4) $H_2S = 1/2\,S_2 + H_2$,

5) $CO + 1/2\,S_2 = COS$,

6) $1/2\,S_2 + O_2 = SO_2$.

The other additional equations taken into account were the material-balance equations for carbon [Eq. (7)] and hydrogen [Eq. (8)]. The fluid contains variable oxygen and sulfur concentrations because of pyrrhotite oxidation. In a closed system, the amount of oxygen incorporated in magnetite corresponds to the amount of sulfur transferred into the fluid, which enabled us to write the third equation [Eq. (9)].

7) $X_{COS} + X_{CO_2} + X_{CO} = 0.5$,

8) $X_{H_2O} + X_{H_2S} + X_{H_2} = 0.5$,

9) $3/4\,(0.5 - \Sigma X_i n_{O,i}) = \Sigma X_i n_{S,i}$,

where X_i is the mole fraction of component i, and $n_{O,i}$ and $n_{S,i}$ are the numbers of oxygen and sulfur atoms in component i. The six equations of the mass-action law for reactions (1)–(6) and three material-balance equations are sufficient to calculate the concentrations of the fluid components. In these calculations, oxygen was taken into consideration in equilibrium equations for variable oxygen fugacity (fO_2). The amount of oxygen in the material-balance equations was neglected because the molar concentration of this component was vanishingly low. The constants of Eqs. (1)–(6) were calculated with regard for the fugacity coefficients of the gas components of the fluid. The system of equations was numerically resolved with the MAPLE software. We have determined that equilibrium is reached at oxygen fugacity fO_2 = QFM + 0.72. In reactions with excess pyrrhotite, 4% H_2O and 1.8% CO_2 are consumed. The fluid generated thereby contains approximately 2 mol % sulfur-bearing components (1.7 mol % H_2S, 0.3 mol % COS, 0.1 mol % SO_2, and 0.03 mol % S_2). The CO and H_2 concentrations reach 0.6 and 0.24 mol %, respectively.

If, instead of using Eq. (9), it is assumed that the oxygen fugacity is constant, the fluid composition can be calculated for a system opened with respect to oxygen. Let fO_2 = QFM − 2, i.e., the oxygen fugacity is buffered by the reaction between the fluid and olivine cumulus. As was mentioned above, this oxygen fugacity is close to that at the CCO buffer at the P–T parameters of the cumulus process in the Yoko-Dovyren intrusion. In this situation, methane cannot be neglected, and it was thus included in the set of the components. The total concentration of the sulfur-bearing gases in the reduced fluid in contact with pyrrhotite decreases to 0.56 mol % (0.48 mol % H_2S, 0.08 mol % COS, 0.67×10^{-7} mol % S_2, and 0.3×10^{-7} mol % SO_2). The concentration of CO in the fluid reaches 10.4 mol %, and this fluid contains 3.1 mol % CH_4 and 4.4 mol % H_2. According to our experimental data, fluid with such a high CO concentration should be able to dissolve much Pt (Simakin et al., 2016).

At oxygen fugacity slightly above the QFM buffer, sulfur concentration in the fluid is relatively high, and the fluid may contain, in addition to hydrogen sulfide, also organo-sulfuric compounds thiols, which are alcohols whose oxygen is substituted for sulfur (such as CH_3SH). The stability of precious-metal compounds with thiols at high P–T parameters is so far known inadequately poorly. At low P–T parameters, thiols form stable complexes with Cd, Ag, and Zn (https://en.wikipedia.org/wiki/Thiol), i.e., with metals typical of the Kholodninskoe deposit, which is situated near the northeastern boundary of the Yoko-Dovyren intrusion (Distanov et al., 1995).

MECHANISMS OF FLUID REDUCTION IN THE CUMULUS OF ULTRAMAFIC INTRUSIONS

Data and considerations presented above can be interpreted as follows. The early skarn-forming processes were associated with silica transfer with the fluid from chert segregations in the dolomite and the crystallization of diopside. Later the fluid removed silica to form the diopside–monticellite zone. During retrogression, the fluid, which was enriched in fluorine and calcium, induced rankinite crystallization. The oxidized V species, the VO^{2+} ion, was formed at the originally high oxygen fugacity in CO_2, which was released at decarbonation reactions (see, for example, Simakin et al., 2012). It can be suggested that the released CO_2 fluid was reduced when reacting with the cumulus olivine and sulfides and enriched in Pt, Ag, and chalcophile elements (As, Cd, and Se). When the reduced CO_2 fluid filtered through the diopside skarn at $700 < T < 950$°C, the bleached zone was produced. The boundary between the zones is sharp. The fluid penetrating into the blue diopside zone deposited Pt and Ag in the rocks. Our blue diopside samples show correlations between the Pt and Ag (as well as As) concentrations at a constant V content. Vanadium concentration in the bleached zone decreases to 7–6 ppm. The low Pt, Ag, and V concentrations in this zone likely indicate that the solubility of these elements in the fluid was high. The unusual composition of amphibole in the plagiolherzolite (see above) confirms that the fluid was rich in vanadium and chromium at a temperature close to 1000°C (the crystallization temperature of the amphibole). The crystallization of the amphibole also suggests that the water mole fraction in the reduced fluid was also high. Characteristics of fluid–magmatic and fluid early postmagmatic interaction are important for understanding the mechanism that produced

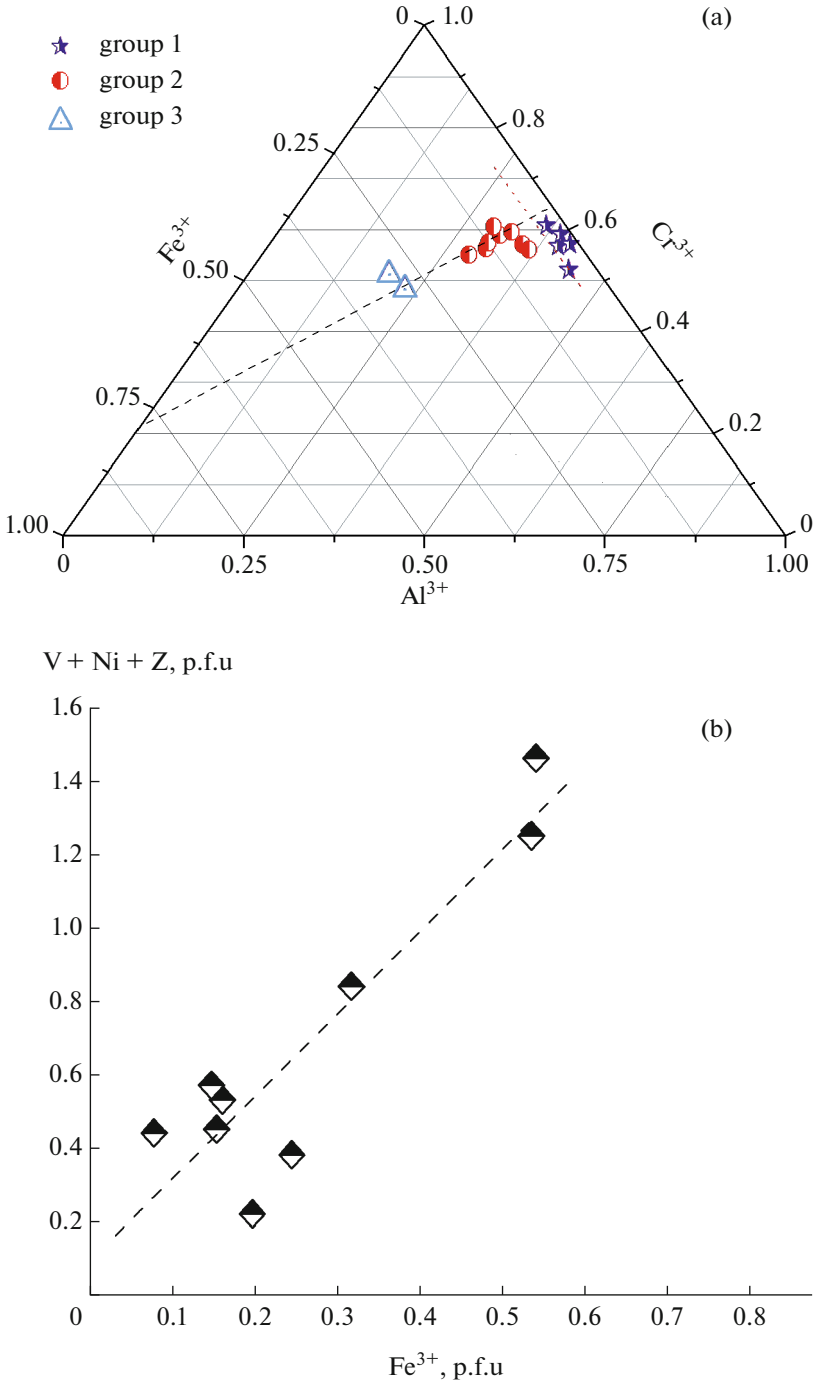

Fig. 7. Composition of spinels from the basal plagioperidotite series of the Yoko-Dovyren massif (Kislov et al., 1995). Subsolidus reaction between the olivine and H_2O–CO_2 fluid is associated with (a) enrichment of the spinel in the magnetite end member (with Cr) (dashed line), the variations along the Cr–Al join correspond to the trend of magmatic fractional crystallization according to (Nikolaev et al., 2017); (b) interaction with fluid sometimes results in spinel enrichment in V and Zn, with the Ni concentration also changing.

ore mineralization of the low-sulfide platiniferous reefs in the Yoko-Dovyren massif (Kislov, 1998). The oxygen fugacity, which was estimated using olivine from the ultramafic part of the massif by high-temperature electrochemistry techniques, was much lower than the QFM buffer (up to QFM – 4) at a subsolidus temperature of 1000°C (Ariskin et al., 2017). This is consistent with the thermodynamic evaluations pre-

sented above. It can be hypothesized that the state of the minerals reflects subsolidus reequilibration under reduced conditions.

The mechanism suggested for fluid reduction is also confirmed by data on the composition of spinel from plagioperidotites and plagiodunites of the Yoko-Dovyren intrusion (Kislov, 1998). As was mentioned in (Nikolaev et al., 2017), spinel is oxidized under subsolidus parameters and is enriched in the magnetite end member (Fig. 7a). The recrystallization of the spinel was associated with its enrichment in Zn, V, and sometimes also Ni, as seen in Fig. 7b.

The list of elements whose concentrations significantly vary in the skarns and their sedimentary protoliths, and which are thus characterized by good solubility in reduced CO_2-bearing fluid, is remarkable in that these elements can form stable carbonyl complexes at low P–T parameters. These elements are Ni, V, Mo, Cr, and Re. The stability of the complexes at high P–T parameters awaits its studying. The Pt solubility in aqueous fluid in the form of chloride complexes is high at high oxygen fugacity (Mungal and Naldrett, 2008), as it also is at low oxygen fugacity in carbon dioxide-bearing fluid (carbonyls, perhaps, with chlorine and sulfur). When the Merensky Reef and the platiniferous reef in the Yoko-Dovyren massif were formed, the oxygen fugacity was reportedly QFM – 2 (Ballhaus and Sylvester, 2000), which suggests the origin of carbonyls. The mechanism suggested above for the reduction of CO_2 fluid when it interacts with olivine in cumulates at a high temperature may be also applicable to layered intrusions (such as Bushveld and Yoko-Dovyren) and the mantle.

CONCLUSIONS

Oxygen fugacity in fluids generated when dolomite interacted with the ultramafic magma of the Yoko-Dovyren massif broadly varied. (1) The blue diopside was formed by early skarn-forming processes at a high oxygen fugacity in the released carbon dioxide, which ensured the origin of the VO^{2+} ion. (2) According to our thermodynamic calculations, the H_2O–CO_2 fluid was reduced to approximately QFM – 2 due to a reaction with the olivine cumulate. The diopside was formed from dolomite at a high silica activity in the fluid, which was caused by dolomite-hosted chert segregations. The low SiO_2 activity in the H_2O–CO_2 fluid, which was buffered by reactions with the ultramafic rocks, caused the transformation of the diopside into monticellite. When reacting with the olivine sulfide-bearing cumulus, the fluid was reduced, and this was accompanied by the synthesis of CO and H_2S and, perhaps, also organo-sulfuric compounds. The blue diopside may have been enriched in Pt (up to 0.2 ppm) when the rocks were reworked by H_2O–CO_2 fluid, which was released at decarbonation reactions and which extracted the metal when interacting with the magma and magmatic cumulus.

ACKNOWLEDGMENTS

The authors thank V.K. Karandashev (Institute of Problems of the Technology of Microelectronics and Ultrapure Materials, Russian Academy of Sciences) for ICP-MS analysis of natural samples. L.Ya. Aranovich (Institute of the Geology of Ore Deposits, Petrography, Mineralogy, and Geochemistry, Russian Academy of Sciences) and A.S. Mekhonoshin (Vinogradov Institute of Geochemistry, Siberian Branch, Russian Academy of Sciences) are thanked for the informative reviews of the manuscript. We highly appreciate constructive criticism expressed by L.Ya. Aranovich, which allowed us to cardinally improve the quality of the thermodynamic calculations. During its final phase, this study was financially supported by the Russian Foundation for Basic Research, project no. 18-05-00597.

REFERENCES

Aird, H.M. and Boudreau, A.E., High-temperature carbonate minerals in the Stillwater Complex, montana, USA, *Contrib. Mineral. Petrol.,* 2013, vol. 166, pp. 1143–1160.

Altukhov, E.N., Gershanik, S.Yu., Glazunov, O.M., et al., Tectonic position and ore potential of mafic-ultramafic rocks of Northern Baikal region, *Geol. Geofiz.,* 1990, no. 6, pp. 56–64.

Ariskin, A.A., Danyushevsky, L.V., Konnikov, E.G., et al., The Dovyren intrusive complex (northern Baikal region, Russia): isotope-geochemical markers of contamination of parental magmas and extreme enrichment of the source, *Russ. Geol. Geophys.,* 2015, vol. 56, no. 3, pp. 411–434.

Ariskin, A.A., Fomin, I.S., Zharkova, E.V., et al., Redox conditions during crystallization of ultramafic and gabbroic rocks of the Yoko–Dovyren Massif (based on the results of measurements of intrinsic oxygen fugacity of olivine), *Geochem. Int.,* 2017, vol. 55, no. 7, pp. 595–607.

Ariskin, A.A., Kostitsyn, Yu.A., Konnikov, E.G., Danyushevskii, L.V., et al., Geochronology of the Dovyren intrusive complex, Northwestern Baikal Area, Russia, in the Neoproterozoic, *Geochem. Int.,* 2013, no. 11, pp. 859–875.

Ariskin, A.A., Kislov, E.V., Danyushevsky, L.V., et al., Cu–Ni–PGE fertility of the Yoko-Dovyren layered massif (Northern Transbaikalia, Russia): thermodynamic modeling of sulfide compositions in low mineralized dunite based on quantitative sulfide mineralogy, *Mineral. Deposita,* 2016, vol. 51, pp. 993–1011.

Ballhaus, C. and Stumpfl, E.F., Sulfide and platinum mineralization in the Merensky Reef: evidence from hydrous silicates and fluid inclusions, *Contrib. Mineral. Petrol.,* 1986, vol. 94, pp. 193–204.

Ballhaus, C. and Sylvester, P., Noble metal enrichment processes in the Merensky Reef, Bushveld Complex, *J. Petrol.,* 2000, vol. 41, pp. 545–561.

Berman, R.G. and Aranovich, L.Y., Optimized standard state and solution properties of minerals, *Contrib. Mineral. Petrol.,* 1996, vol. 126, nos. 1–2, pp. 1–24.

Boudreau, A.E. and Meurer, W.P., Chromatographic separation of the platinum-group elements, base metals, gold and sulfur during degassing of a compacting and solidifying igneous crystal pile, *Contrib. Mineral. Petrol.,* 1999, vol. 134, pp. 174–185.

Canil, D. and Fedortchouk, Y., Olivine–liquid partitioning of vanadium and other trace elements, with application to modern and ancient picrites, *Can. Mineral.,* 2001, vol. 39, pp. 319–330.

Distanov, E.G. and Kovalev, K.R., Kholodninskoe stratiform sulfide–base metal deposit, *Mestorozhdeniya Zabaikal'ya* (Transbaikalian Deposits), Chita; M.: *Geoinformmark*, 1995, Vol. 1, pp. 83–93.

Doroshkevich, A., Sklyarov, E., Starikova, A., et al., Stable isotope (C, O, H) characteristics and genesis of the Tazheran brucite marbles and skarns, Olkhon region, Russia, *Mineral. Petrol.,* 2017, vol. 111, pp. 399–416.

Duan, Z.H. and Zhang, Z.G., Equation of state of the H_2O–CO_2 system up to 10 GPa and 2573 K: molecular dynamics simulations with ab initio potential surface, *Geochim. Cosmochim. Acta,* 2006, vol. 70, no. 9, pp. 2311–2324.

Ferry, J.M., Ushikubo, T., and Valley, J.W., Formation of forsterite by silicification of dolomite during contact metamorphism, *J. Petrol.,* 2011, vol. 52, no. 9, pp. 1619–1640.

French, B.M. and Eugster, H.P., Experimental control of oxygen fugacities by graphite–gas equilibriums, *J. Geophys. Res.,* 1965, vol. 70, no. 6, pp. 1529–1539.

Frey, M. and Robinson, D., *Low-Grade Metamorphism,* Oxford: Blackwell Science, 1999.

Frost, B.R., Introduction to oxygen fugacity and its petrologic importance, *Rev. Mineral.,* 1991, vol. 25, pp. 1–9.

Ganino, C., Arndt, N.T., Chauvel, C., et al., Melting of carbonate wall rocks and formation of the heterogeneous aureole of the Panzhihua intrusion, china, *Geosci. Front.,* 2013, vol. 4, pp. 535–546.

Holland, T.J.B. and Powell, R., An internally consistent thermodynamic data set for phases of petrological interest, *J. Metamorph. Geol.,* 1998, vol. 16, pp. 309–343.

Jones, L.C., Rosenbauer, R., Goldsmith, J.I., et al., Carbonate control of H_2 and CH_4 production in serpentinization systems at elevated P-Ts, *Geophys. Rev. Lett.,* 2010, vol. 37, L14306; doi 10.1029/2010GL043769

Kislov, E.V., *Ioko-Dovyrenskii rassloennyi massiv* (Yoko-Dovyren Layered Massif), BNTs SO RAN, 1998.

Konnikov, E.G., Tsygankov, A.A., and Vrublevskaya, T.T., *Baikalo-Muiskii vulkano-plutonicheskii poyas: strukturno-veshchestvennye kompleksy i geodinamika* (Baikal–Muya Plutonic Belt: Lithotectonic Complexes and Geodynamics), Moscow: GEOS, 1999.

Konnikov, E.G., Meurer, W.P., Neruchev, S.S., et al., Fluid regime of platinum group elements (PGE) and gold-bearing reef formation in the Dovyren mafic-ultramafic layered complex, eastern Siberia, Russia, *Mineral. Deposita,* 2000, vol. 35, pp. 526–532.

Lepage, L.D., ILMAT: an Excel worksheet for ilmenite–magnetite geothermometry and geobarometry, *Comput. Geosci,* 2003, vol. 29, no. 5, pp. 673–678.

Mathez, E.A., Magmatic metasomatism and formation of the Merensky Reef, Bushveld Complex, *Contrib. Mineral. Petrol.,* 1995, vol. 119, pp. 277–286.

Mungal, J.E. and Naldrett, A.J., Ore deposits of the platinum-group elements, *GeoScienceWorld in Elements,* 2008, vol. 4, pp. 253–258.

Nikolaev, G.S., Bychkov, K.A., and Ariskin, A.A., Modeling olivine–spinel and olivine–spinel–sulfide cotectics during crystallization of ultramafic magmas, *Ul'tramafit-mafitovye kompleksy: geologiya, stroenie, rudnyi potentsial: materialy V Mezhdunarodnoi konferentsii (Gremyachinsk, 2–6 sentyabrya 2017 g.)* (Ultramafic–mafic Complexes: Structure and Ore Potential. Proceedings of 5th International Conference, Gremyachinsk, 2017), Ulan-Ude: Izdvo Buryatskogo gosuniversiteta, 2017, pp. 196–198.

Pertsev, N.N. and Shabynin, L.I., *Skarn, carbonate, and brucite xenoliths of the Yoko–Dovyren massif, Kontaktovye protsessy i orudenenie v gabbro-peridotitovykh intruziyakh* (Contact Processes and Mineralization in the Gabbro–Peridotite Intrusions), Moscow: Nauka, 1978, pp. 85–96.

Putirka, K.D., Igneous thermometers and barometers based on plagioclase + liquid equilibria: tests of some existing models and new calibrations, *Am. Mineral.,* 2005, vol. 90, nos. 2–3, pp. 336–346.

Robie, R.A., Hemingway, B.S., and Fisher, J.R., Thermodynamic properties of minerals and related substances at 298.15 K and 1 bar (10^5 pascals) pressure and at higher temperatures, *US Geol. Surv. Bull.,* 1978, no. 1452.

Sack, R.O. and Ghiorso, M.S., Chromian spinels as petrogenetic indicators: thermodynamics and petrological applications, *Am. Mineral.,* 1991, vol. 76, pp. 827–847.

Satake, M. and Mido, Y., *Chemistry of transition elements*, New Delhi: Discovery Publishing House, 2010.

Shi, P. and Saxena, S.K., Thermodynamic modeling of the C–H–O–S fluid system, *Am. Mineral.,* 1992, vol. 77, nos. 9–10, pp. 1038–1049.

Simakin, A.G. and Shaposhnikova, O.Yu., Novel amphibole geobarometer for high-magnesium andesite and basalt magmas, *Petrology,* 2017, vol. 25, no. 2, pp. 226–239.

Simakin, A.G., Salova, T.P., and Bondarenko, G.V., Experimental study of magmatic melt oxidation by CO_2, *Petrology,* 2012, vol. 20, no. 7, pp. 593–606.

Simakin, A.G., Salova, T.P., Gabitov, R.I., et al., Dry CO_2–CO fluid as an important potential deep earth solvent, *Geofluids,* 2016, vol. 16, pp. 1043–1057.

Simakin A.G., Devyatova V.N., Salova T.P., et al., Properties of reduced carbon dioxide fluid: evidence from experimental and thermodynamic modeling, *Dokl. Earth Sci.,* 2018, vol. 478, pp. 70–73.

Sun, S.-S. and McDonough, W.F., Chemical and isotopic systematics of oceanic basalts: implications for mantle composition and processes, *Magmatism in Ocean Basins,* Saunders, A.D. and Norry M.J., *Geol. Soc. London Spec. Publ.,* 1989, pp. 313–345.

Wenzel, T., Baumgartner, L.P., Brugmann, G.E., et al., Partial melting and assimilation of dolomitic xenoliths by mafic magma: the Yoko-Dovyren intrusion (north Baikal Region, Russia), *J. Petrol.,* 2002, vol. 43, no. 11, pp. 2049–2074.

http://models.kl-edi.ac.cn/models/h2oco2/index.htm.

https://earthref.org/GERM.

https://en.wikipedia.org/wiki/Thiol.

http://melts.ofm-research.org/CalcForms/index.html.

Translated by E. Kurdyukov